Modification of Electrical and Optical Properties by Incorporating Mn, Ta and Nb Dopants into TiO_2-based Thin layer Utilizing Powder-based Physical Vapor Deposition (PPVD) Technique

K. A. Mas'oad[a], N. A. Sukrey[a], M. Rizwan[b] and A.R. Bushroa[a,c,*]

[a]Department of Mechanical Engineering, Universiti Malaya, 50603 Kuala Lumpur, Malaysia

[b]Department of Metallurgical Engineering, Faculty of Chemical and Process Engineering NED University of Engineering and Technology, 70503 Karachi, Pakistan

[c]Centre of Advanced Manufacturing and Material Processing (AMMP), Department of Mechanical Engineering, Universiti Malaya, 50603 Kuala Lumpur, Malaysia

***Corresponding authors:**

bushroa@um.edu.my

materialist.riz@gmail.com

Abstract

Powder-based Physical Vapor Deposition (PPVD) was utilized to deposit doped TiO_2 thin layers, to modify electronic and optical properties. The modification was performed using several dopants (MnO_2, Ta_2O_5, Nb_2O_5) at different concentrations (0.05 and 0.1 mol%) respectively. The structural characterization by FESEM revealed that the size of the grain varied with respect to the dopants. The sample doped at lower concentration demonstrated larger crystallite size than the sample doped at higher concentration. This trend is consistent with the measured grain size of the doped thin layer samples. The nonlinearity coefficient (α) and breakdown voltage (at lower ranges) enhanced as the dopant concentration in the TiO_2 lattice increased due to the reduction of grain size. While, the optical properties of the doped TiO_2 thin layers with respect to energy bandgap demonstrated enhancement trend with the addition of the dopant, as revealed by UV-Vis reflectance analysis. The enhancement of electrical and optical properties is attributed to the formation of barrier layer surrounding the grains, which in return increased the conductivity of the doped TiO_2 thin layers sample. This study demonstrates the feasibility of the PPVD method in producing a dense thin layer structure for potential applications in optical and electrical sectors.

Keywords: titanium dioxide; powder physical vapor deposition; breakdown voltage; nonlinear coefficient; energy bandgap; adhesion strength;

[DOI: 10.22068/ijmse.3707]

1 Introduction

Titanium dioxide (TiO_2) has rapidly emerged as a widely studied metal oxide for photocatalyst application. Applications of TiO_2 photocatalysts include; water treatment and organic pollutant degradation [1-3], air purification [4, 5], self-cleaning surfaces [6-8], carbon dioxide (CO_2) conversion to hydrocarbon fuels [9, 10], as well as hydrogen production by water splitting [11, 12]. TiO_2 offers several advantages, such as: outstanding biocompatibility, low cost, non-toxicity, stable physical and chemical properties, as well as high availability. However, TiO_2 has been extensively researched in order to enhance its usefulness and efficiency [13, 14].The relatively large band gap (3.0 eV in rutile phase, and 3.2 eV in anatase phase) limits their photoactivity which can be activated with the presence of ultraviolet (UV) light only [15]. As a result, this situation reduces its efficiency in utilizing the solar irradiation since, only 5% of the whole solar spectrum comprises of UV light [16].

Thus, few strategies have been attempted to modify the band gap structure which in return contribute to the enhanced photoactivity. Generally, the research conducted focuses in finding solution with low-cost, environment friendly, as well as excellent visible light driven photocatalytic activity [17]. The key to expanding the photoactivity range of TiO_2 relies on the modification of their defect chemistry through doping strategy, which in return shifts the absorption range of TiO_2 towards visible light spectrum [18, 19]. Doping strategy is an extensively explored technique, in regards to the TiO_2 modification. There are four types of TiO_2 dopant, listed as the self-doping with reduced Ti^{3+}, nonmetal dopant, metal dopant, as well as co-dopant [20]. In view of the development of TiO_2 as photocatalyst, doping is reported together with the crystal growth, shape control, and surface modification as the approaches to achieve an optimized photo response activity [21-23].

While, in the semiconductor related studies, doping process is also employed to control the formation of Schottky barrier which contributes to the electrical nonlinearity. This electrical nonlinearity would be highly beneficial for the further application as voltage surge protector which requires the high nonlinear properties [24, 25]. The diffusion of dopant ions (Ca^{2+}) into the TiO_2 lattice and occupies the Ti^{4+} site, subsequently produces two electrons [26]. As a result, one free oxygen vacancies is produced in order to create the electric charge balance. Larger the Ca^{2+} doping concentration, higher the number of oxygen vacancies. This enhanced oxygen vacancies will improve the electron movement, which subsequently increases the grain conductivity. The relatively larger ionic radius and lower valence of Ca^{2+} compared to Ti^{4+} attributes to the lower solubility of Ca^{2+} within the TiO_2 lattice. Accordingly, the excess Ca^{2+} will segregate at the grain boundary, decreasing the elastic strain energy, and therefore enhancing the resistivity between the grain boundaries. This dopant segregation phenomenon also reduces the crystallite sizes and increases the TiO_2 rutile phase presence, which contributes to high stability of TiO_2 photocatalytic activity [27].

Doping by using aluminum (Al), copper (Cu), molybdenum (Mo), and tungsten (W) leads to the narrowing of the band gap, which subsequently shifts the photoactivity towards the visible light spectrum [28]. The introduction of these dopant ions into the TiO_2 lattice introduces a localized band, near the valence band that reduces the band gap energy. The number of oxygen vacancies increase which subsequently provides donor states below the

[DOI: 10.22068/ijmse.3707]

conduction band (CB). This results, the enhancement of photocatalytic reaction [29]. This phenomenon on the modified band gap structure is also beneficial for the wettability properties of TiO_2-based thin layers for anti-fogging and self-cleaning application. TiO_2 comprises of Ti^{4+} and O^{2-} ions. When TiO_2-based thin layer is exposed to ultraviolet light, electrons from the valence band (VB) are promoted to the CB, leaving a positively charged hole. The Ti^{4+} ions are reduced to Ti^{3+}, and the oxygen atoms are ejected, contributing to the formation of oxygen vacancies. The water molecules (H_2O) will occupy these oxygen vacancies, resulting in the absorbed OH. This phenomenon will elevate the hydrophilicity of the TiO_2 surface to superhydrophilicity, resulting in improved wettability and anti-fogging capabilities [30]. However, this photoactivity is highly dependent on the presence of UV, which was previously mentioned as one of the limitations of TiO_2.

Thus, doping plays an essential role in the improvement of optical as well as electrical characteristic. Careful consideration must be taken into account, on the selection of the type as well as the concentration of dopant. Through this research, the behavior of the TiO_2-based thin layer was studied as a function of dopants (Mn_2O_3, Ta_2O_5, Nb_2O_5) with two different concentrations (0.05 and 0.10 mol%) added into the lattice structure. The structural, compositional, optical, and electrical behavior with respect to nonlinearity and voltage breakdown is evaluated in details. Furthermore, the mechanical strength of the deposited thin layer in regards of their adhesion strength has also been evaluated.

[DOI: 10.22068/ijmse.3707]

2 Experimental procedure

The schematic structure of the thin layer varistor of this research is presented in Figure 1. The doped TiO_2 based thin layer was deposited, as a single layer on the silicon wafer (1 0 0).

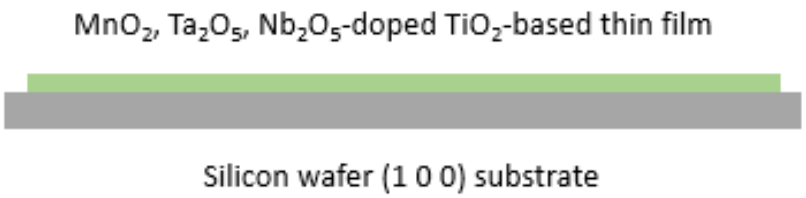

Figure 1 The schematic structure of the TiO_2 based thin film varistor

2.1 Substrate and target preparation

A polished p-type silicon wafer with (1 0 0) orientations was cut into small coupons (15 mm X 15 mm) by using a diamond tip cutter. Subsequently, the small coupons were then ultrasonically cleaned in the distilled water and ethanol bath for 20 minutes. This cleaning step was carried out, following the cutting process to eliminate the grease and contaminants. These unwanted contaminants need to be removed prior to the deposition process to ensure the direct adhesion of the sputtered doped TiO_2 target on the silicon substrate.

The TiO_2 powder (Sigma Aldrich, US) was mixed with respective dopant powder (Mn_2O_3, Ta_2O_5, or Nb_2O_5) (Sigma Aldrich, US) at respective weight, to produce the 99.5 mol% and 99.0 mol% composition of TiO_2 to the dopant. The details of the dopant composition in TiO_2 are as tabulated in *Table 1*. The TiO_2 powder of 300 mesh was mixed prior to the deposition process by using the planetary ball milling machine (Retsch PM 100) for 3 hours with speed set at 300 rpm. This mixing step is to ensure the uniform distribution and homogenous mixing of TiO_2 and dopant powder. The doping of the TiO_2 takes place during the deposition process, in which the powder target was exposed to high temperature with the plasma generated in the chamber.

Table 1 Details on the type and concentration of dopant in TiO_2

Sample	Designation	Composition
$Mn_{0.05}$	A1	0.05 mol% MnO_2 + 99.5 mol% TiO_2
$Mn_{0.10}$	A2	0.10 mol% MnO_2 + 99.0 mol% TiO_2
$Ta_{0.05}$	B1	0.05 mol% Ta_2O_5 + 99.5 mol% TiO_2
$Ta_{0.10}$	B2	0.10 mol% Ta_2O_5 + 99.0 mol% TiO_2
$Nb_{0.05}$	C1	0.05 mol% Nb_2O_5 + 99.5 mol% TiO_2
$Nb_{0.10}$	C2	0.10 mol% Nb_2O_5 + 99.0 mol% TiO_2

[DOI: 10.22068/ijmse.3707]

2.2 Deposition process

The deposition was carried out in an unconventional custom-made powder magnetron sputtering system. The powder mixture of TiO_2 and its respective dopants was weighted at approximately 45 g and carefully patted on the target holder of around 8 cm in diameter. The powders were levelled to get all contained in the holder. A cut of the silicon wafer was nicely placed above the target with the distance of around 8 cm. After placing the powder target and the substrate, the chamber was closed and screwed tightly to reduce any air leaking. The evacuation was started with a rough pump and followed with a turbo molecular pump reaching low vacuum of around 4 x 10^{-3} Pa to ensure that the sputtered atoms can travel without colliding with other gas molecules. After that, Argon gas was purged into the chamber. The Argon gas volume was set at 25 sccm. Once the gas was stable at this amount, the radio frequency generator was increased up to 200 W and adjusted to get a consistent plasma density. At this moment, the working pressure was obtained at around 0.5 Pa. For all set of experiments, RF power, Argon gas flow and deposition time were kept constant with 200 W, 25 sccm and 3 hours, respectively as shown in Table 2. The variable manipulated was the amount of dopant composition as shown in Table 1. Once the deposition time was over, RF generator was shut down and the Nitrogen gas was inserted to start chamber ventilation. After the chamber has reached ventilation state, chamber section was opened and the substrate that had been deposited was taken out and safely placed in the plastic box.

Table 2 The process parameter of the PPVD technique

Parameter	Value
RF power (W)	200
Deposition time (hour)	3
Argon gas flow (sccm)	25.0

2.3 Coating characterization

2.3.1 Structural and phase composition

X-ray diffraction (XRD, D/Max-2200) with CuK_α radiation was used to analyse the crystal phase of the thin layer samples. From the XRD spectrum obtained, the crystallite size was calculated by implementing Scherrer equation as follows;

$$D = \frac{K\lambda}{\beta cos\theta} \qquad \text{(Equation 2.1)}$$

Where D is the crystallite size (nm), K is Scherrer constant, usually 0.94 for spherical crystallites with cubic symmetry, λ is the X-ray wavelength, CuK_α=1.54178 Å, β is the line broadening at full width half maximum (FWHM) in radians and θ is the Bragg's angle in degree, half of 2θ. The diffraction patterns were recorded in the diffraction angles 2θ ranging from 20° to 70°. Then, the crystal phase of deposited thin layer samples was determined from the diffraction patterns.

[DOI: 10.22068/ijmse.3707]

2.3.2 Microstructure and elemental distribution

The thin layer varistor microstructure and morphology was observed via Field Emission Scanning Electron Microscopy (FESEM) (ZEISS SIGMA 300 VP Microscopy, Germany). The elemental composition and distribution throughout the thin layer samples was identified from the Energy Dispersive X-Ray Analysis (EDS) analysis.

2.3.3 Mechanical properties

The mechanical properties of the deposited thin layer were evaluated by the adhesion strength of the thin layer. Micro scratch testing was carried out by applying a linearly increasing load from 0 to 2500 mN along a 1000 μm scratch length. The scratch track was observed by using the optical microscope to determine the failure mode of the coating. The load that causes a coating delamination defines the critical load (L_C) of the coating.

2.3.4 Electrical properties

The current-voltage (I-V) curve was measured using Keithley Electrometer (4200 SCS). Silver electrodes were sputtered on both surfaces of the ceramic for electrical properties evaluation. Applied voltage ranging from -10V to 10V with 0.05 step size was set on the electrometer prior to measurement process. The obtained I-V curve was further analysed for the electrical performance evaluation in view of nonlinear coefficient (α) and breakdown voltage (V_B). The α and V_B was calculated according to Equation 2.2 and 2.3.

$$\alpha = \frac{\log (I_2/I_1)}{\log (V_2/V_1)} \qquad \text{(Equation 2.2)}$$

Where V_1 and V_2 are the voltages at the currents I_1 and I_2 respectively.

$$V_B = n v_B \qquad \text{(Equation2.3)}$$

Where v_B is the voltage barrier at a grain boundary. This measured value was utilized to evaluate the electrical performance of doped thin layer samples.

2.3.5 Optical properties

Optical behaviour of the doped TiO_2 thin layer samples was evaluated from the Ultraviolet-Visible Spectroscopy (UV-Vis) analysis. The reflectance against wavelength from UV-Vis raw data is fully utilized to obtain the energy bandgap (E_G) value. The optical reflectance coefficient (F(R)) was calculated according to Equation 2.4.

$$(F(R)) = \frac{K}{S} \qquad \text{(Equation 2.4)}$$

[DOI: 10.22068/ijmse.3707]

Where K and S are the absorption and scattering coefficients respectively. The photon energy (hv) was further calculated from the relationship of frequency (v) to the light's speed (c) and wavelength (λ) as follows;

$$hv = \frac{h}{2\pi}(2\pi f) = hf = \frac{hc}{\lambda} \qquad \text{(Equation 2.5)}$$

where h is the Planck's constant (h = 6.62601 X 10^{-34} Js), c = 2.9979 X 10^{8} m/s, and λ is the wavelength in nm. In this study, all the calculations involved to obtain the E_G value is carried out by utilizing a graphing and analysis software, OriginLab. The E_G of each of the thin layer samples was calculated from the extrapolation of linear fitted line on $(F(R)hv)^2$ against photon energy graph.

[DOI: 10.22068/ijmse.3707]

3 Results and discussion

3.1 Structural and phase composition

The XRD analysis reveals that all the samples exhibited a single phase TiO_2 rutile structure, and no secondary phases are observed. This observation is due to the complete substitution of Mn, Ta, and Nb dopant into TiO_2 lattice during the deposition process. The average crystallite size obtained from the Scherrer equation is tabulated in *Table 3*. The trend of average crystallite size decreases with the increase in dopant concentration. The $Ta_{0.10}$ doped TiO_2 exhibits the smallest crystallite size at 153.28±13.47 nm.

Table 3 The average crystallite size of each sample

Sample	Average crystallite size (nm)
$Mn_{0.05}$	192.68 ± 14.64
$Mn_{0.10}$	189.71 ± 23.25
$Ta_{0.05}$	187.89 ± 30.00
$Ta_{0.10}$	153.28 ±13.47
$Nb_{0.05}$	174.78 ± 24.41
$Nb_{0.10}$	164.28 ± 6.56

The XRD spectrum was analysed via X'Pert Highscore software. The spectrum shows that all samples are illustrated by similar pattern of peaks. The typical XRD spectrum of all samples showed that there're only two significant peaks observed along 2θ from 5° to 90°. These two peaks are confined between 68° to 70°. Figure 2 reveals the existence of these peaks. The highest one is prevalent at 69.32°, revealing it as the rutile phase of TiO2. Theoretically, the phase transition usually occurs at temperature ranging from 600 to 700 °C, contributing to the changes of anatase to rutile [31]. In this research, the deposition process was conducted in the PPVD chamber in which the magnetron was designed to primarily attract and accumulate the electron in the vicinity of the target and the substrate. Therefore, it is postulated that high impact of atoms and molecules during the deposition process may increase the temperature of the surface layer of the substrate. It eventually rises the temperature that allows the transition of the phases.

Therefore, the original anatase phase of TiO2 transformed to rutile phase could be expected. Apart from the main rutile phase of TiO2, it is hypothesised that the dopant peaks could be observed as well. However due to the capability of the XRD machine, the peak is too low to be detected and thus not significant in the illustrated spectrum.

[DOI: 10.22068/ijmse.3707]

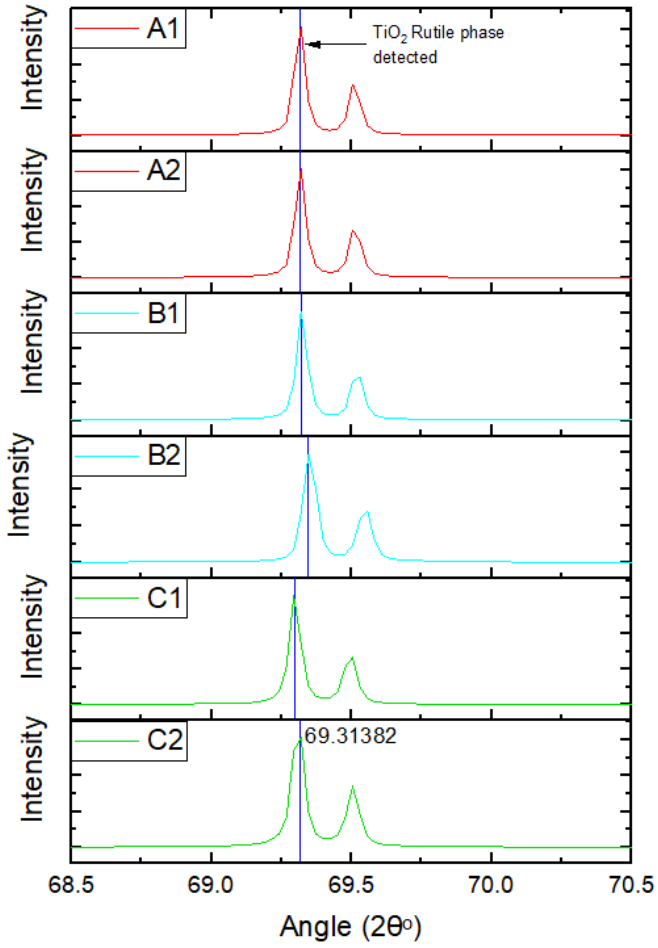

Figure 2 The XRD spectrums of the doped TiO_2 thin films

3.2 Morphological and elemental distribution

The FESEM image illustrates the differences of grain size and structure produced with different dopants. The line intercept method is used to measure the grain size. *Figure 4* illustrates the FESEM images for every sample, while *Table 4* tabulates the calculated average grain size. From the calculated values, the different concentration significantly affects the grain size of the particle. The trend reveals that the higher dopant concentration produces smaller grains. The thin layered sample with 0.10 mol% exhibits smaller grain sizes compared to the samples produced with 0.05 mol% dopant concentration. The smaller the grain size, the more formation of grain boundaries, which subsequently enhances the nonlinear electrical properties of the thin layer in varistor application. An observation from previous research reveals the decrease of grain size with the addition of dopant, which in returns reduces the total electrical conductivity of TiO_2 doped with ZrO_2 varistor [32] [31]. This observation is consistent with the obtained results of this study.

[DOI: 10.22068/ijmse.3707]

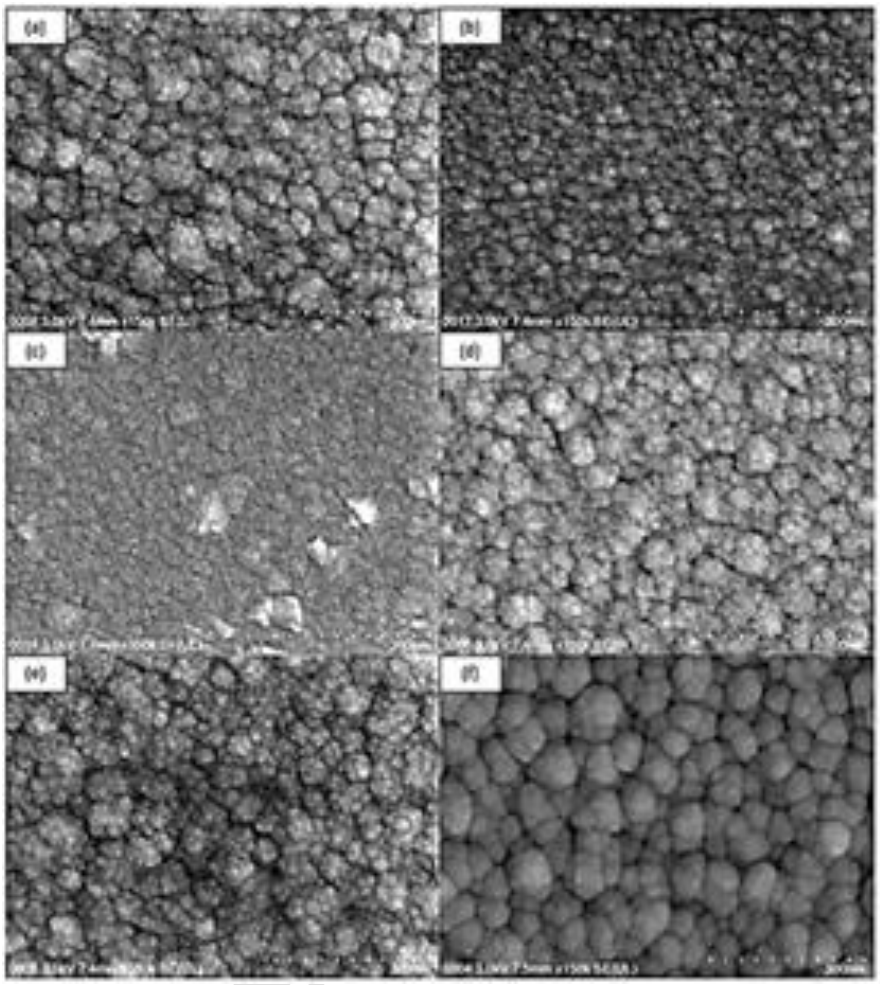

Figure 3 The FESEM images of doped TiO_2 thin films with; (a) $Mn_{0.05}$, (b) $Mn_{0.10}$, (c) $Ta_{0.05}$, (d) $Ta_{0.10}$, (e) $Nb_{0.05}$, and (f) $Nb_{0.10}$.

Table 4 The grain size average, after taking five different dimensions from the micro image of each sample

Sample	Average grain size (nm)
$Mn_{0.05}$	462.07 ± 33.40
$Mn_{0.10}$	343.01 ± 28.11
$Ta_{0.05}$	485.10 ± 41.75
$Ta_{0.10}$	391.52 ± 44.28
$Nb_{0.05}$	543.66 ± 50.57
$Nb_{0.10}$	527.35 ± 51.42

Further analysis by EDS confirms (as presented in *Figure 4*) the presence of dopant, hence proving that the mixing of two different powders, TiO_2 and dopant (MnO_2, Ta_2O_5 & Nb_2O_5) has taken place successfully and subsequently deposited on the substrate.

[DOI: 10.22068/ijmse.3707]

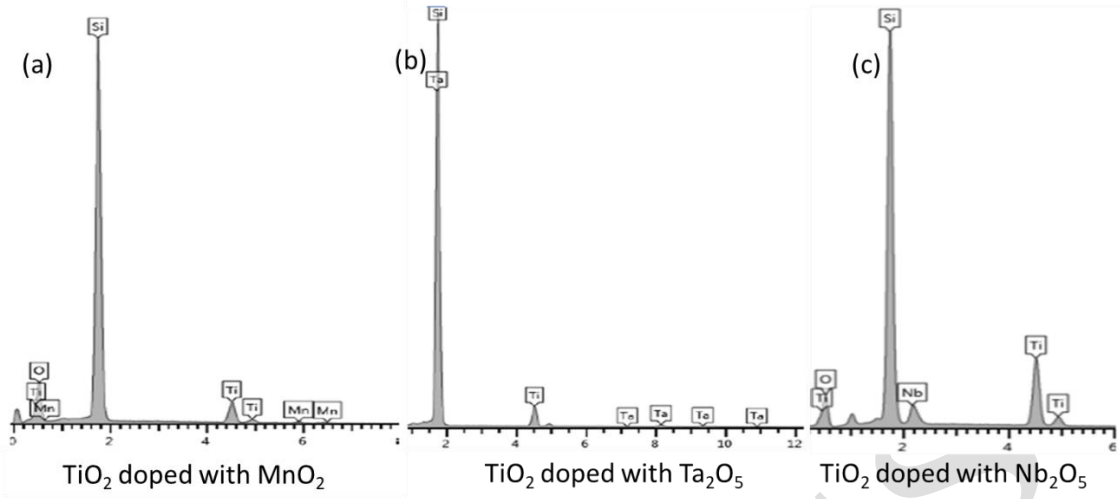

Figure 4 EDS result of each sample

3.3 Mechanical properties

The adhesion strength of the deposited TiO_2 ceramics layer was measured in this research to evaluate the mechanical strength of each thin layer. Generally, the properties of varistor sample were studied in view of their structural, optical, and electrical behaviours only. The mechanical evaluation of the thin layer is studied in this research to evaluate the PPVD technique in developing functional thin layer with excellent mechanical properties.

A 1000 μm scratch was produced on the coated sample of a typical 3 - 5 microns thickness. The image was observed under optical microscope. The critical load was determined at the point of coating failure, revealing the substrate underneath. The scratch test was done on three samples ($Mn_{0.05}$, $Ta_{0.05}$, and $Nb_{0.05}$) to evaluate the adhesion strength of the TiO_2 based thin layers. *Table 5* tabulates the result of the scratch test with respect to their failure length and critical load for the coating to fail.

Table 5 The adhesion strength of the TiO_2-based thin layers sample.

Sample	Failure length and critical load (L_C)
$Mn_{0.05}$	Fails at 836.59 with load 1310.60 mN
$Ta_{0.05}$	Fails at 842.63 with load 1321.62 mN
$Nb_{0.05}$	Fails at 833.76 with load 1304.64 mN

The recorded result of scratch test does not reflect a significant influence of dopants type on the adhesion of deposited TiO_2 thin layer. The doping strategy on TiO_2-based thin layer does not seem to be a key factor in influencing their adhesion strength. This insignificant adhesion strength can be due to the same processing parameter of PPVD set during the deposition process.

Higher RF power will result to higher energy of sputtered atoms on the substrate surface. The flow rate of the working Ar gas into the deposition chamber also plays an

[DOI: 10.22068/ijmse.3707]

important role by increasing the deposition rate, which subsequently influencing the density and adhesion of the thin layers. However, since the RF power and Ar flow rate throughout the sample's preparation is maintained at 200 W and 25.0 sccm, the energy of sputtered atoms also does not vary. Thus, subsequently contributes to this indifferent adhesion strength of the deposited doped TiO_2 thin layers.

3.4 Electrical properties

The I-V characteristic for all samples is illustrated in *Figure 5*. The nonlinear coefficient increases when the concentration of the dopant is increased from 0.05 to 0.1 mol%. The doping with 0.1 mol% Ta_2O_5 demonstrates a good nonlinear coefficient α=1.56. The V_B of the varistor increases with the decrease in grain size, which demonstrates a result of the increasing doping concentration. The resistivity of the TiO_2 grains increases with the increase of doping amount due to the increasing grain boundaries.

The value for the nonlinear coefficient for MnO_2 is lower than the Ta-doped varistor sample. The increase in concentration of the dopant successfully contributes to the nonlinear coefficient improvement. The increase in concentration of the dopant MnO_2, could decrease the grain size [33]. In other perspective, SEM images show that different material produce different grain size. This occurred due to different ionic radii for each three elements. Mn^{2+}, Ta^{5+}, and Nb^{5+} has ionic radii of 0.07nm, 0.064nm and 0.065nm, respectively. While Ti^{4+} has an ionic radius 0.061nm. All of three elements have almost similar ionic radii that helps the dopant ions to dissolve into the TiO_2 lattice easily. This promotes the formation of the grain in TiO_2. However, when the dopant concentration increases, the size of grain starts to decrease as demonstrated by the average grain and crystallite size results. Thus, dopant concentration plays an important role in modifying the performance of TiO_2 samples.

The formation of the grain boundary or the depletion layers hinder the movement of the electrons transmitting. Hence, the amount of dopant increases the formation of this layer, while decreasing the grain size. More barriers will be formed to hinder the electrons. The breakdown voltage is decreased as the concentration of the dopant increases. The addition of this particular dopant can decrease the resistivity of a specific grain, including the breakdown voltage.

The decrease in the grain resistance promotes the formation barriers at the grain boundaries and simultaneously enhances the nonlinear coefficient. The ionic radius from each particular ion also affects the grain growth and also the breakdown voltage. The closest ionic radius to Ti^{4+} which is Ta^{5+} and Nb^{5+}, produced

lower breakdown voltage compared to Mn^{2+}, *Table 5*.

[DOI: 10.22068/ijmse.3707]

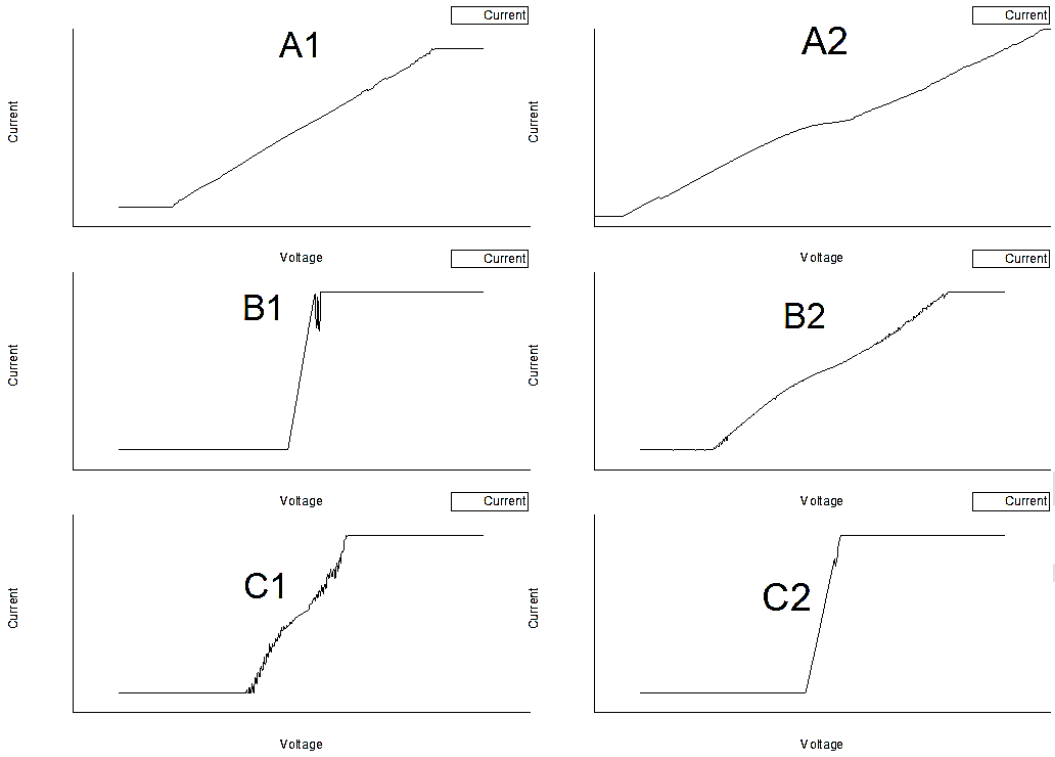

Figure 5 Voltage-current curves for A1, A2, B1, B2, C1, and C2 respectively.

Table 5 The calculated values of nonlinear coefficient (α) and voltage breakdown (V_B) of each sample

Sample	Nonlinearity Coefficient, α	Breakdown Voltage, V_B (V)
$Mn_{0.05}$	1.0260	0.95
$Mn_{0.10}$	1.1989	0.85
$Ta_{0.05}$	1.3204	1.10
$Ta_{0.10}$	1.5679	0.70
$Nb_{0.05}$	0.7491	0.45
$Nb_{0.10}$	0.9959	0.10

It can be found that the thin layer varistor with 0.1 mol% Ta_2O_5 has the best nonlinear electrical property with highest nonlinear coefficient, α 1.56 with breakdown voltage of 0.7 Vmm^{-1}. This thin layer varistor may be beneficial for low voltage protection application that requires smaller voltage clamping dimension. The value of the nonlinear coefficient may reach its maximum and then decrease with increasing the dopant concentration. This observation is attributed by the hindrance of electron movement with the decrease in grain size as well as enhanced barrier layer. This phenomenon has significantly affected the electrical properties of these doped TiO_2 thin layers.

[DOI: 10.22068/ijmse.3707]

3.5 Optical properties

The optical properties evaluation in view of the reflectance spectrum obtained from UV-Vis analysis reveals the alteration of optical bandgap energy. The Tauc plots were constructed to determine the respective energy bandgap (E_G) of each thin layer samples, *Figure 6*. The value of EG is tabulated in the following table, *Table 6*.

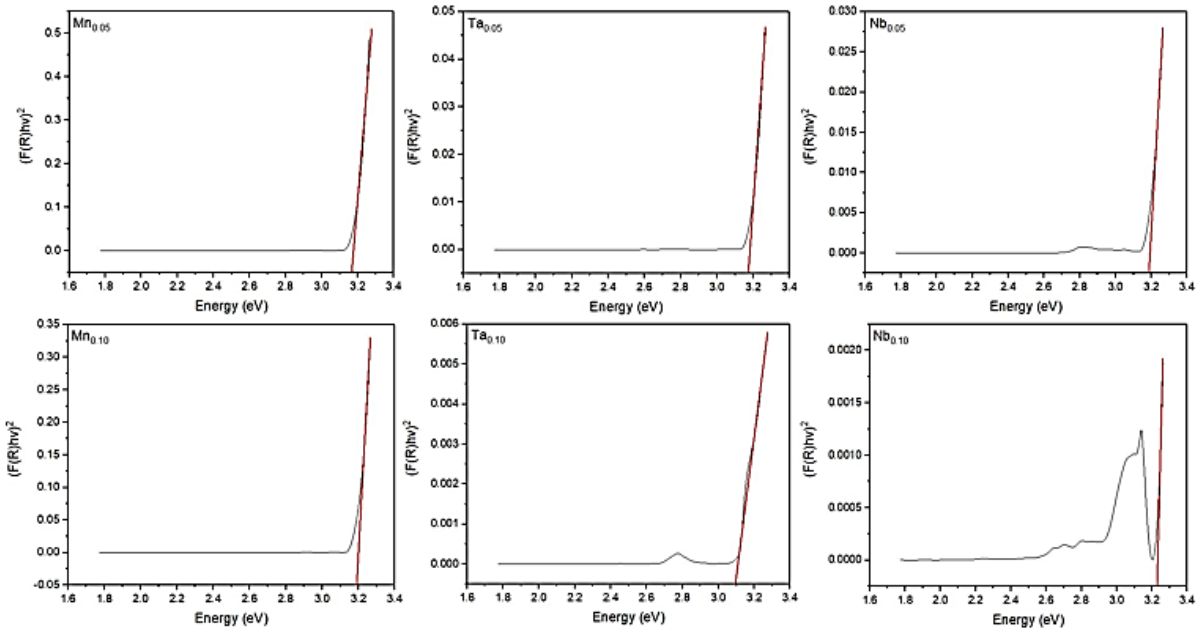

Figure 6 Tauc plots of respective doped TiO_2 thin films

Table 6 The E_G values of each of the doped TiO_2 thin layers

Sample	Energy bandgap, E_G
$Mn_{0.05}$	3.17
$Mn_{0.10}$	3.15
$Ta_{0.05}$	3.16
$Ta_{0.10}$	3.09
$Nb_{0.05}$	3.19
$Nb_{0.10}$	3.23

The evaluation of E_G reveals that the trend is consistent according to their grain size and electrical properties. Doped sample with 0.10 mol% Ta_2O_5 exhibits the lowest energy bandgap, indicating the effective enhancement of optical properties through doping strategy. The consistency of this E_G with other results demonstrated the direct correlations of structural modification, which subsequently influences the electrical as well as the optical properties of the doped samples.

[DOI: 10.22068/ijmse.3707]

4 Conclusion

The TiO_2 thin layer doped with three different materials MnO_2, Ta_2O_5, and Nb_2O_5 at two different concentrations, 0.05 and 0.10 mol% were successfully developed via the unconventional PVD method. The influence of the type of dopant and concentration on the TiO_2 doped varistor was studied in view of their structural, elemental distribution, and electrical performance characterization. The increase in dopant concentration has effectively enhanced the nonlinear coefficient, grain resistance, as well as energy bandgap due to the reduction of grain sizes of the lattice system. The TiO_2 varistor sample with 0.10 mol% Ta_2O_5 possesses the best electrical and structural properties. The feasibility of the unconventional PVD method to produce an electrical functioning thin layer has been demonstrated through this research.

5 References

1. Hua, L., Z. Yin, and S. Cao, *Recent advances in synthesis and applications of carbon-doped TiO2 nanomaterials.* Catalysts, 2020. **10**(12): p. 1431. **https://doi.org/10.3390/catal10121431**
2. Zhang, J., et al., *Aerosol processing of Ag/TiO2 composite nanoparticles for enhanced photocatalytic water treatment under UV and visible light irradiation.* Ceramics International, 2022. **48**(7): p. 9434-9441. https://doi.org/10.1016/j.ceramint.2021.12.140
3. Cerrato, E., et al., *The role of Cerium, Europium and Erbium doped TiO2 photocatalysts in water treatment: A mini-review.* Chemical Engineering Journal Advances, 2022. **10**: p. 100268. https://doi.org/10.1016/j.ceja.2022.100268
4. Patil, S.B., et al., *Recent advances in non-metals-doped TiO2 nanostructured photocatalysts for visible-light driven hydrogen production, CO2 reduction and air purification.* International Journal of Hydrogen Energy, 2019. **44**(26): p. 13022-13039. https://doi.org/10.1016/j.ijhydene.2019.03.164
5. Mamaghani, A.H., F. Haghighat, and C.-S. Lee, *Role of titanium dioxide (TiO2) structural design/morphology in photocatalytic air purification.* Applied Catalysis B: Environmental, 2020. **269**: p. 118735. https://doi.org/10.1016/j.apcatb.2020.118735
6. Jalvo, B., et al., *Antimicrobial and antibiofilm efficacy of self-cleaning surfaces functionalized by TiO2 photocatalytic nanoparticles against Staphylococcus aureus and Pseudomonas putida.* Journal of hazardous materials, 2017. **340**: p. 160-170. https://doi.org/10.1016/j.jhazmat.2017.07.005
7. Lukong, V., et al., *Deposition and characterization of self-cleaning TiO2 thin films for photovoltaic application.* Materials today: proceedings, 2022. **62**: p. S63-S72. https://doi.org/10.1016/j.matpr.2022.02.089
8. Won, Y., K. Schwartzenberg, and K.A. Gray, *TiO2-based transparent coatings create self-cleaning surfaces.* Chemosphere, 2018. **208**: p. 899-906. https://doi.org/10.1088/1757-899X/1053/1/012061
9. Xu, M., et al., *One-step in-situ synthesis of porous Fe3+-doped TiO2 octahedra toward visible-light photocatalytic conversion of CO2 into solar fuel.* Microporous and Mesoporous Materials, 2020. **309**: p. 110539. https://doi.org/10.1016/j.micromeso.2020.110539
10. Wang, D., et al., *In situ chloride-mediated synthesis of TiO2 thin film photoanode with enhanced photoelectrochemical activity for carbamazepine oxidation coupled with simultaneous cathodic H2 production and CO2 conversion to fuels.* Journal of Hazardous Materials, 2021. **410**: p. 124563. https://doi.org/10.1016/j.jhazmat.2020.124563

[DOI: 10.22068/ijmse.3707]

11. Jung, S.-C., et al., *Photocatalytic hydrogen production using liquid phase plasma from ammonia water over metal ion-doped TiO2 photocatalysts.* Catalysis Today, 2022. **397**: p. 165-172. https://doi.org/10.1016/j.cattod.2021.11.010
12. Park, Y.-K., et al., *Characteristics of hydrogen production by photocatalytic water splitting using liquid phase plasma over Ag-doped TiO2 photocatalysts.* Environmental Research, 2020. **188**: p. 109630. https://doi.org/10.1016/j.envres.2020.109630
13. Khatun, N., et al., *Stable anatase phase with a bandgap in visible light region by a charge compensated Ga–V (1: 1) co-doping in TiO2.* Ceramics International, 2020. **46**(7): p. 8958-8970. https://doi.org/10.1016/j.ceramint.2019.12.143
14. Muhammad, B., et al., *RF nitrogen plasma irradiation of metal-doped TiO2 nanowire arrays as an effective technique for improved light transmission and optical bandgap manipulation.* Chemical Physics, 2020. **538**: p. 110922. https://doi.org/10.1016/j.chemphys.2020.110922
15. Ebrahimi, S., et al., *Improving optoelectrical properties of photoactive anatase TiO2 coating using rGO incorporation during plasma electrolytic oxidation.* Ceramics International, 2019. **45**(2): p. 1746-1754. https://doi.org/10.1016/j.ceramint.2018.10.057
16. Zhou, F., et al., *N-doped TiO2/sepiolite nanocomposites with enhanced visible-light catalysis: Role of N precursors.* Applied Clay Science, 2018. **166**: p. 9-17. https://doi.org/10.1016/j.clay.2018.08.025
17. Zong, L., et al., *The preparation of superhydrophobic photocatalytic fluorosilicone/SiO2–TiO2 coating and its self-cleaning performance.* Journal of Coatings Technology and Research, 2021. **18**(5): p. 1245-1259. https://doi.org/10.1007/s11998-021-00485-x
18. Kuang, J., et al., *Surface plasma Ag-decorated single-crystalline TiO2− x (B) nanorod/defect-rich g-C3N4 nanosheet ternary superstructure 3D heterojunctions as enhanced visible-light-driven photocatalyst.* Journal of colloid and interface science, 2019. **542**: p. 63-72. https://doi.org/10.1016/j.jcis.2019.01.124
19. Zhang, Y., et al., *Interfacial defective Ti3+ on Ti/TiO2 as visible-light responsive sites with promoted charge transfer and photocatalytic performance.* Journal of Materials Science & Technology, 2022. **106**: p. 139-146. https://doi.org/10.1016/j.jmst.2021.06.081
20. Chen, J., et al., *Recent progress in enhancing photocatalytic efficiency of TiO2-based materials.* Applied Catalysis A: General, 2015. **495**: p. 131-140. https://doi.org/10.1016/j.apcata.2015.02.013
21. Park, H., et al., *Surface modification of TiO2 photocatalyst for environmental applications.* Journal of Photochemistry and Photobiology C: Photochemistry Reviews, 2013. **15**: p. 1-20. https://doi.org/10.1016/j.jphotochemrev.2012.10.001
22. Padmanabhan, N.T., et al., *Graphene coupled TiO2 photocatalysts for environmental applications: A review.* Chemosphere, 2021. **271**: p. 129506. https://doi.org/10.1016/j.chemosphere.2020.129506
23. Dong, Y. and F. Meng, *Effect of triblock copolymers on crystal growth and the photocatalytic activity of anatase TiO 2 single crystals.* RSC advances, 2020. **10**(54): p. 32400-32408. https://doi.org/10.1039/d0ra05965j
24. Liao, X., Y. Pu, and D. Zhu, *Synergistic effect of co-doping of nano-sized ZnO and Nb2O5 on the enhanced nonlinear coefficient of TiO2 varistor with low breakdown voltage.* Journal of Alloys and Compounds, 2021. **886**: p. 161170. https://doi.org/10.1016/j.jallcom.2021.161170

[DOI: 10.22068/ijmse.3707]

25. Peng, F. and D. Zhu, *Effect of sintering temperature and Ho2O3 on the properties of TiO2-based varistors.* Ceramics International, 2018. **44**(17): p. 21034-21039. https://doi.org/10.1016/j.ceramint.2018.08.139
26. Sendi, R.K., *Electric and dielectric behaviors of (Ca, Ta)-doped TiO2 thick film varistor obtained by screen printing.* Results in physics, 2018. **8**: p. 758-763. https://doi.org/10.1016/j.rinp.2018.01.012
27. Gandelman, H., et al., *Interface excess on Sb-doped TiO2 photocatalysts and its influence on photocatalytic activity.* Ceramics International, 2021. **47**(1): p. 619-625. https://doi.org/10.1016/j.ceramint.2020.08.169
28. Sukrey, N.A., Bushroa, A.R. & Rizwan, M. *Dopant incorporation into TiO_2 semiconductor materials for optical, electronic, and physical property enhancement: doping strategy and trend analysis.* J Aust Ceram Soc, 2024. **60**, 563–589. https://doi.org/10.1007/s41779-023-00958-9
29. Liao, W., et al., *Electrochemically self-doped TiO2 nanotube arrays for efficient visible light photoelectrocatalytic degradation of contaminants.* Electrochimica Acta, 2014. **136**: p. 310-317. https://doi.org/10.1016/j.electacta.2014.05.091
30. Garlisi, C. and G. Palmisano, *Radiation-free superhydrophilic and antifogging properties of e-beam evaporated TiO2 films on glass.* Applied Surface Science, 2017. **420**: p. 83-93. https://doi.org/10.1016/j.apsusc.2017.05.077
31. Byrne, C., et al., *New approach of modifying the anatase to rutile transition temperature in TiO 2 photocatalysts.* RSC advances, 2016. **6**(97): p. 95232-95238. https://doi.org/10.1039/C6RA19759K
32. Tekeli, S., et al., *Microstructural and electrical conductivity properties of cubic zirconia doped with various amount of titania.* Journal of Achievements in Materials and Manufacturing Engineering, 2007. **25**(2): p. 39-43. https://doi.org/10.1007/s10008-008-0530-6
33. Gong, Y., et al., *Nonlinear electrical properties of MnO 2-doped TiO 2 capacitor varistor ceramics.* Journal of Materials Science: Materials in Electronics, 2015. **26**: p. 7232-7237. https://doi.org/10.1007/s10854-015-3349-9

Declaration of interests

The authors declare no competing financial interests or personal relationships that influence the work reported in this paper.

[DOI: 10.22068/ijmse.3707]